applied sciences

Article

Magnetic Permeability Perturbation Testing for Internal Axial Cracks in Small-Diameter Thick-Walled Steel Pipes

Xueyu Zhao, Zhiyang Deng *, Zhiheng Yu, Tingyi Li and Xiaochun Song

Key Lab of Modern Manufacture Quality Engineering, Hubei University of Technology, Wuhan 430068, China
* Correspondence: dzy@hust.edu.cn

Abstract: Special geometric features and complex working environments render the internal defects of small-diameter thick-walled steel pipes "easy to expand, difficult to detect". In this paper, a magnetic permeability perturbation testing (MPPT) method is proposed to assess the internal axial cracks of small-diameter thick-walled steel pipes. The mechanism of the MPPT method and its corresponding probe and magnetizer are introduced, and its feasibility is verified through a series of simulations and experiments. Experiments conducted using different sizes of small-diameter thick-walled pipes show that this method offers good performance with respect to the detection of internal axial cracks. Additionally, both diameter and wall thickness significantly affect the MPPT signal. To a certain extent, a greater wall thickness or a smaller diameter brings about a weaker signal. This method does not benefit from the lift-off effect, nor is it limited by the skin effect, which has great practical value as a supplement to the evaluation of thick-walled steel pipes.

Keywords: magnetic permeability perturbation testing; small-diameter; thick-walled steel pipes; internal axial cracks

check for updates

Citation: Zhao, X.; Deng, Z.; Yu, Z.; Li, T.; Song, X. Magnetic Permeability Perturbation Testing for Internal Axial Cracks in Small-Diameter Thick-Walled Steel Pipes. *Appl. Sci.* **2023**, *13*, 7107. https://doi.org/10.3390/app13127107

Academic Editors: José António Correia and Bruno Brunone

Received: 4 April 2023
Revised: 9 June 2023
Accepted: 12 June 2023
Published: 14 June 2023

1. Introduction

Small-diameter thick-walled steel pipes are widely used in power stations (including nuclear power stations) and other areas. The long-term operation of these pipelines under complex working conditions will lead to various types of defects on the internal walls of the pipes, which pose great potential risks to the reliability and safety of the structure [1–3]. The circumferential stress in the pipe wall is about twice the scale of the axial stress, and axial cracking is more dangerous than circumferential cracking under the influence of creep. Actual inspection conditions often require the inspection of internal wall defects on the external wall of a pipe. Therefore, the detection of axial cracks inside small-diameter thick-walled steel pipes is extremely important.

The nondestructive testing methods for internal wall defects in thick-walled steel pipes mainly include radiographic testing (XT), ultrasonic testing (UT), magnetic flux leakage testing (MFL), eddy current testing (ECT), the use of an electromagnetic acoustic transducer (EMAT), the transient test-based technique (TTBT), etc. The presentation of defect information via radiographic inspection mainly relies on two-dimensional projection, and it is difficult to obtain the specific depth of a defect [4]. Conventional ultrasonic testing provides good penetration depth but usually relies on couplants to achieve better acoustic coupling, and wave mode transitions in small-diameter thick-walled tubes are more complex [5,6]. The ECT method is mostly used to detect surface and near-surface defects [7], and internal inspection is usually not applicable to in-service pipelines [8]. Pulsed eddy current testing (PECT) [9–12] and remote-field eddy current testing (RFECT) [13–16] use the perturbation of eddy currents, and their penetration depth in high-permeability carbon steel materials is greatly reduced. The MFL testing method uses magnetic field perturbations caused by defects, which are affected by the "magnetic shielding effect" of the pipe wall, and its detection sensitivity gradually decreases with the increase in pipe wall thickness [17–23]. Electromagnetic acoustic transducers (EMATs) are suitable for detecting wall-thinning defects, but they are limited by a low efficiency of energy transfer [24,25]. TTBT detects leaks in pipelines through pressure changes and offers high sensitivity, but it is susceptible to environmental changes such as temperature changes and changes in the medium inside the pipeline [26,27].

Ferromagnetic materials exhibit significant non-linear magnetization characteristics under an external magnetic field. In our previous study, we found that ferromagnetic materials inevitably generate permeability perturbation in the DC magnetization state [28]. Based on the mechanism of magnetization or permeability change of ferromagnetic materials, Y Gotoh achieved the detection of internal wall defects through the co-excitation of DC and AC for differential permeability testing [29]. Sophian A designed an improved magnetizer consisting of a DC coil and a U-shaped permanent magnet [30]. Li Erlong used DC-magnetization-based eddy current array testing to quantify the inner surface defects of steel plates [31]. Wu Jianbo proposed a method of scanning induction thermal imaging systems using a DC bias, which relies on effective permeability changes [32].

This paper proposes an MPPT method for the detection of axial cracks in the internal walls of small-diameter thick-walled pipes. Section 1 introduces the MPPT mechanism and the method for detecting axial cracks in the internal wall of the steel pipe. Section 2 investigates the effect of the diameter of a pipe on the distribution characteristics of a steel pipe's magnetic permeability perturbation (MPP) and the signal amplitude. Section 3 verifies the feasibility of the MPPT method through a series of experiments and analyzes the effects of pipe diameter on the detection signal. Section 4 discusses some details of the detection method. The conclusions and prospects for future work are summarized in Section 5.

2. Mechanism

In isotropic ferromagnetic materials, the relationship between $\vec{B}$ and $\vec{H}$ is both nonlinear and defined by hysteresis. $\vec{B}$ is not a single-valued function of $\vec{H}$, and its variation also depends on the magnetization properties of the ferromagnetic material employed. The permeability $\mu_f(\mu = f(H))$ will first reach a maximum with increasing magnetic field strength and then decrease due to saturation. When a material containing defects is magnetized by a static magnetic field, the magnetic lines of force are obstructed by the defect, allowing the magnetic lines of force to preferentially pass over the defect and become squeezed. The magnetic field around the defect is unevenly distributed, which is called magnetic field perturbation, as shown in Figure 1. The magnetic fields in the above-crack region and the far-crack region are $\vec{H}_{DST}$ and $\vec{H}_{non}$, where $H_{DST} > H_{non}$ [28]. According to the nonlinear $\mu - H$ curve, the magnetic permeability of the above-crack area differs from that of the far-crack area, and it changes from μ to $\mu + \Delta\mu$, which is called magnetic permeability perturbation (MPP).

As shown in Figure 1, DC magnetization is used to actively excite MPP. The pipe is rotated along the magnetization direction, and a fixed position probe loaded through AC excitation induces the eddy current field on the external wall of the pipe. The regions of MPP cause changes in eddy current distribution, resulting in changes in the secondary magnetic field received by the probe. In order to maximize the detection sensitivity of the signal, the receiving coils and excitation coils are distributed along the circumference of the pipe directly above the defect. The probe has a differential structure, which is oriented close and perpendicular to the sample to be tested.

As shown in Figure 2, there is an axial defect in the internal wall of the pipe. Figure 2a,b show the MPP distribution of defects when the steel pipe is rotated to different circumferential positions, respectively. As shown in the red circle data in the figure, the MPP above the defect is lower than that of the near-defect area. If the perturbation region reaches the sensitivity range of the probe, the probe will immediately generate a differential signal.

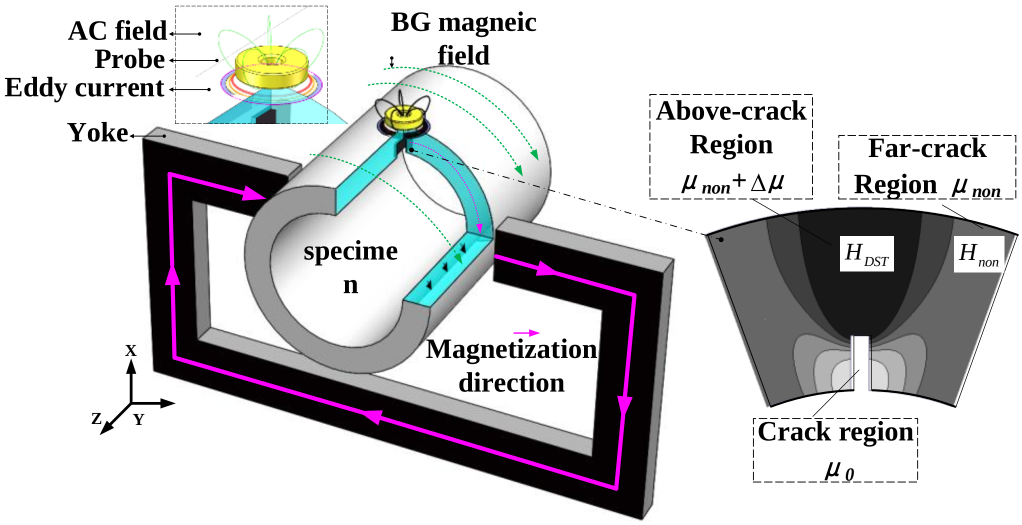

Figure 1. Schematic diagram of the MPPT principle.

With respect to the steel pipe's (X-Y) cross-section, MPP occurs above the defects, and the MPP created by the internal wall defects is concentrated in the near-crack area. As shown in Figure 3, the MPP of region III is directly affected by the external diameter of the pipe. At the same time, the combined effect of the defect size, pipe diameter, and wall thickness determines the final MPP of region III.

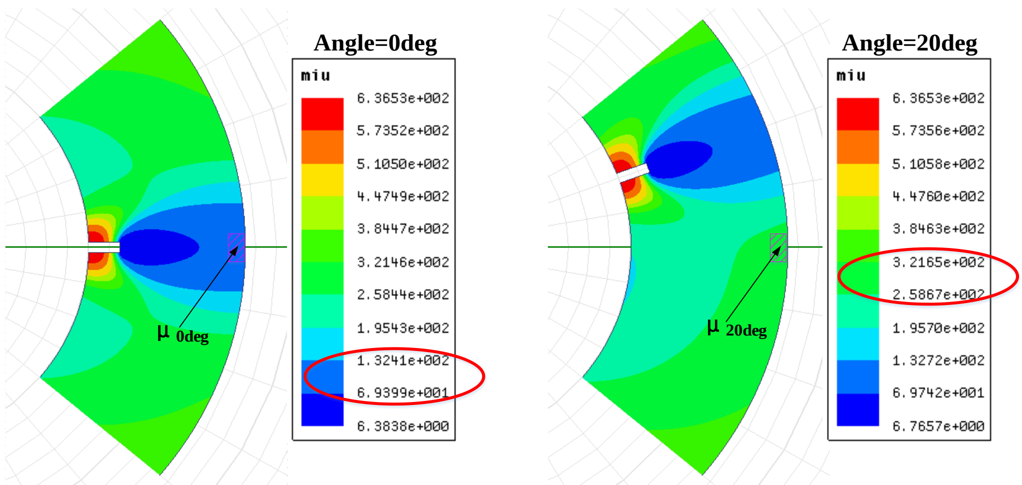

(a) (b)

Figure 2. Schematic diagram of permeability distribution. (**a**) shows the MPP distribution of defects when the pipe is 0 degrees. (**b**) shows the MPP distribution of defects when the pipe is rotated to 20 degrees.

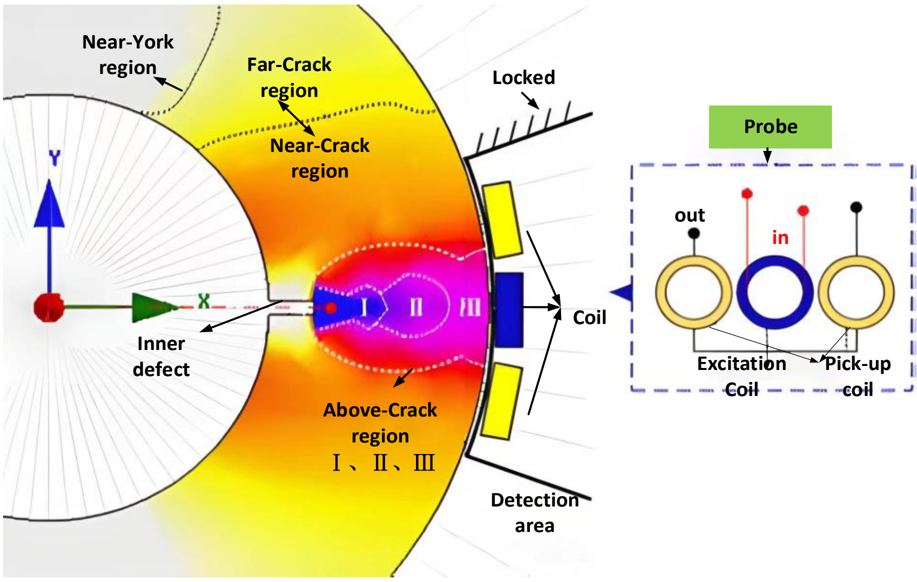

Figure 3. Schematic diagram of the MPPT method.

3. Simulation

3.1. FEA Model of MPPT for Small-Diameter Thick-Walled Steel Pipes

This section presents a finite element analysis (FEA) model built in Ansoft Maxwell to verify the theoretical analysis. The generation of MPPT signals for axial defects in steel pipes is a dynamic process. Figure 4a shows the composition and mesh division of the two-simulation dimensional model, which mainly consists of a magnetic yoke, a direct current coil, an excitation coil, and a receiving coil. The steel tube is located between the upper and lower poles, and the magnetic field generated by the DC coil passes through the steel tube and then through the left yoke to form a magnetic circuit. In Figure 4b, the gap between the sample pipe and the magnetic pole shoe is 5 mm, and the lift-off of the probe is 0.5 mm. In the mesh division, the steel pipe mesh and the probe coil mesh are refined by the traditional adaptive mesh function of the Ansoft Maxwell 16 software in order to improve calculation quality. The magnetization curve of No. 45 steel is used to represent the ferromagnetic material properties in the simulation, assuming that μ_r is isotropic. Table 1 details the parameters required in the simulation and Figure 5 shows the magnetization curves of the materials required in the simulation.

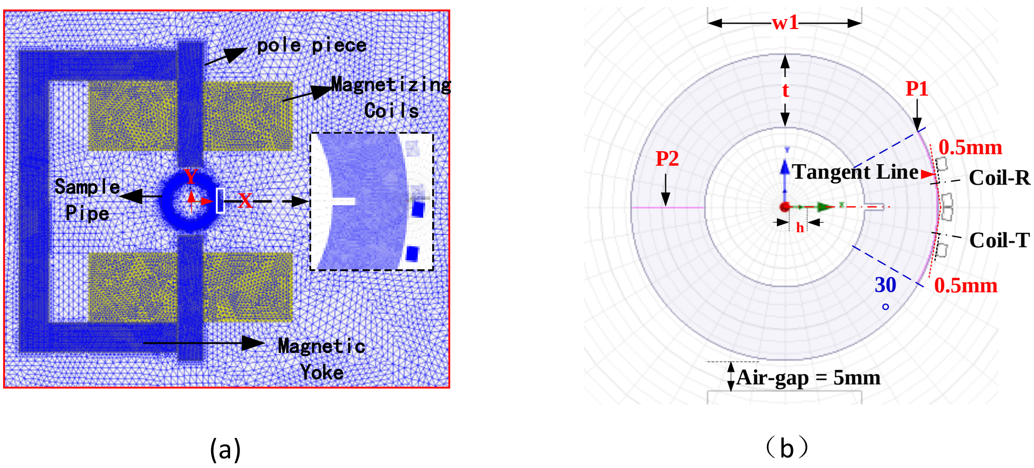

Figure 4. Simulation diagram. (**a**) Models and meshes; (**b**) geometric parameters.

Table 1. Simulation parameter settings.

Parts	Parameter
Excitation coil	Excitation frequency = 50 kHz Voltage = 5 V Number of turns = 100 turns Inner diameter = 4 mm Outside diameter = 8 mm
Magnetized coils	Magnetizing current = 5.5 A N = 3200
Detection coil	Turn Ratio = 100 turns Inner diameter = 4 mm Outside diameter = 8 mm R = 4 Ω; L = 90 µH
Steel pipe material	Material = No. 45 Maximum permeability μ_r = 675
Defects in the inner wall	Width = 1 mm Depth = 1 mm, 1.5 mm

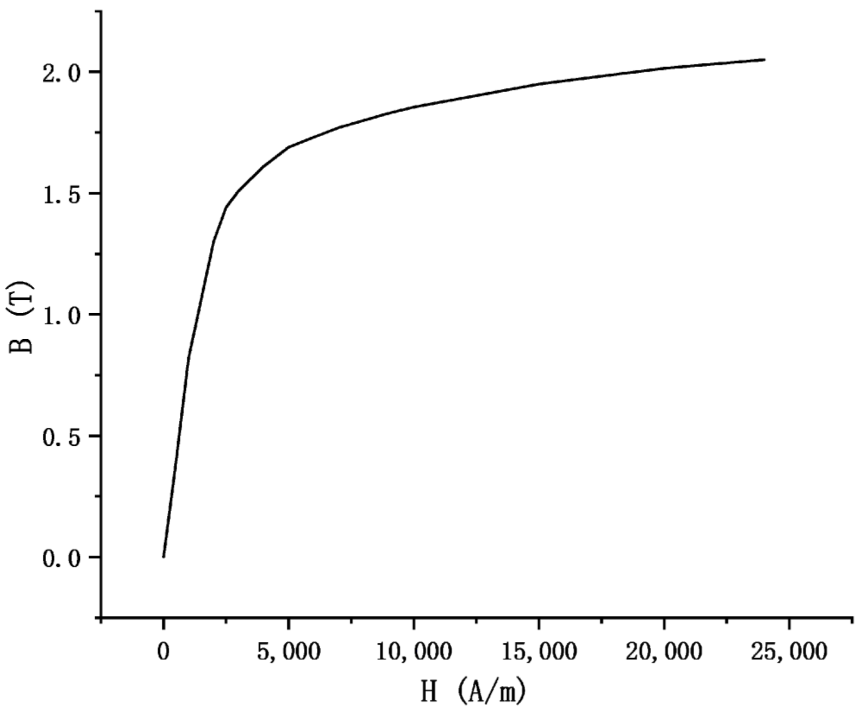

Figure 5. Steel magnetization curve.

3.2. MPP of Axial Cracks of Different Diameters

The simulation results of the φ50 mm × 8 mm steel pipe under different excitation currents are shown in Figure 6. Figure 6a–e show the cloud of the permeability distribution above the defect, and Figure 6g–k reflect the current density variation below the probe. When the magnetizing current is small, the MPP caused by the axial defect in the internal wall is weak, which has a small impact on the eddy current distribution. When the excitation current is strong enough, the MPP causes an effective eddy current perturbation in the surface layer of the steel pipe.

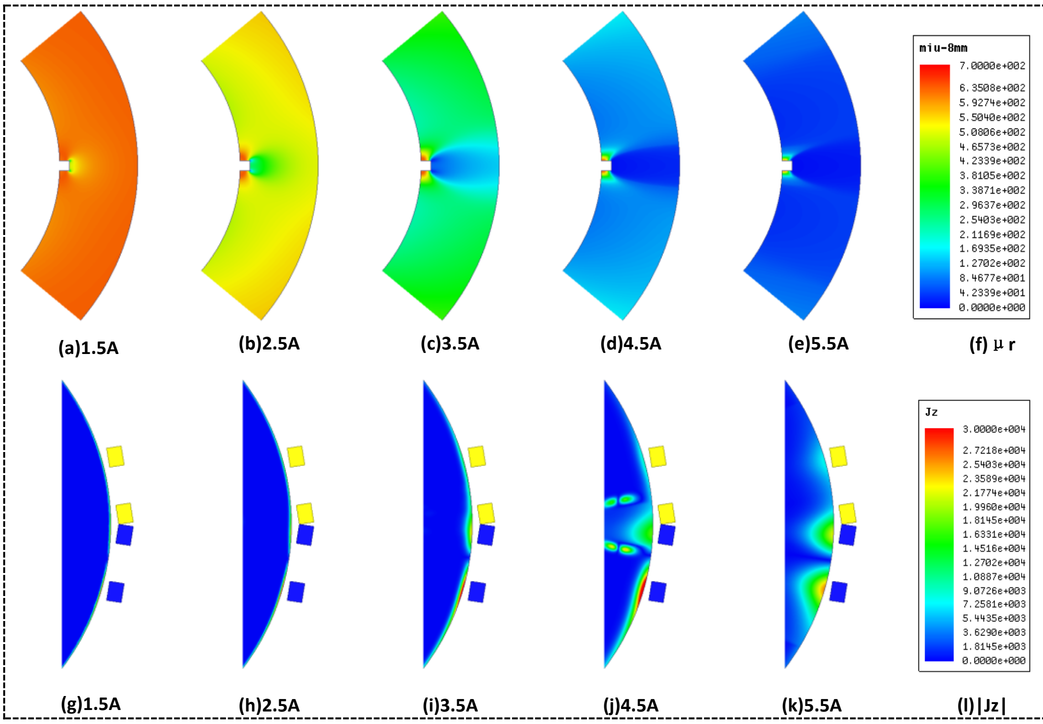

Figure 6. Characteristics of MPP and eddy current distribution at different magnetizing currents.

The maximum induced voltage of the probe is obtained every time the defect passes directly through the probe, as shown in Figure 7a. The changes in MPP under different magnetization currents while other parameter conditions remain unchanged are shown in Figure 7b. The voltage signal gradually increases with the enhancement of the excitation current at different excitation currents, and the voltage signal peaks around 4.5A and then gradually decreases with the enhancement of the excitation current. ΔVpp is the peak-to-valley value of the signal.

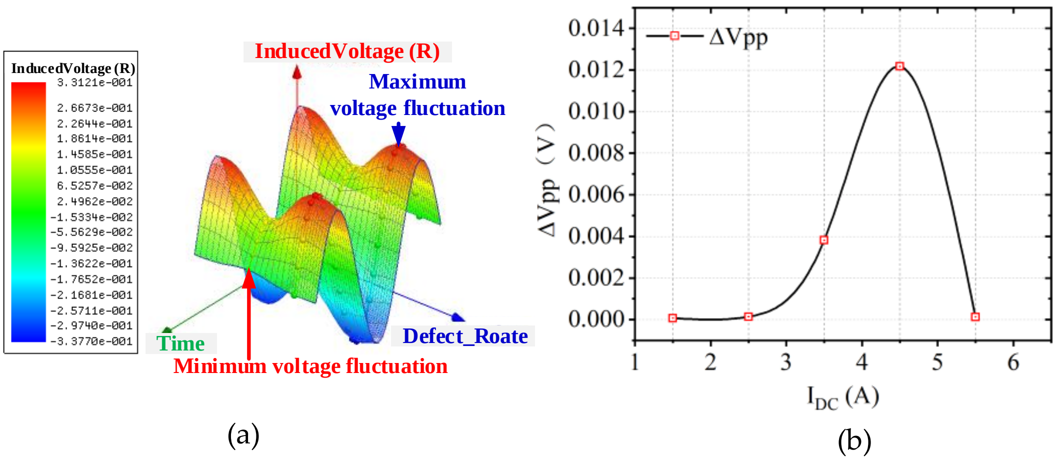

Figure 7. Signal diagram: (**a**) Signal features; (**b**) effect of DC current on the signal.

3.3. Effect of Diameter on MPPT Signal

As shown in Figure 8, the baseline value of the curve decreases as the external diameter of the steel pipe increases, and the concave feature of the signal becomes weaker. For the steel pipes with the same outer radius, the larger the internal diameter of the pipe, the more significant the differences in the MPP of the defect.

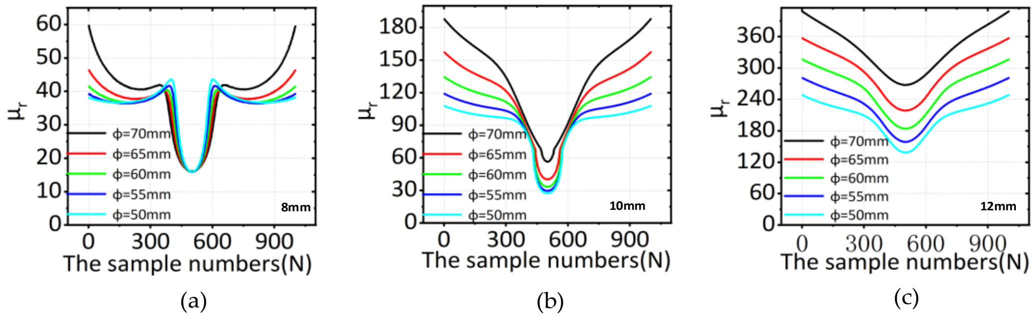

Figure 8. MPP curves at different external diameters of pipes. (**a**) shows the curves of MPP for different external diameter variation at wall thickness of 8 mm, (**b**) shows the curves of MPP for different external diameter variation at wall thickness of 10 mm and (**c**) shows the curves of MPP for different external diameter variation at wall thickness of 12 mm.

Simulation studies were conducted for three wall thickness cases of 8 mm, 10 mm, and 12 mm. The corresponding magnetizing current densities are 2.2×10^5 A/m^2, 2.86×10^5 A/m^2, and 3.49×10^5 A/m^2, respectively, for obtaining the approximate same magnetization degree of the steel pipe. The outer diameters φ of the pipes used at each wall thickness are 50 mm, 55 mm, and 60 mm, respectively. The external diameter of the pipe remains the same, and only the internal diameter is changed. The ΔVpp of the signals are extracted and fitted, as shown in Figure 9.

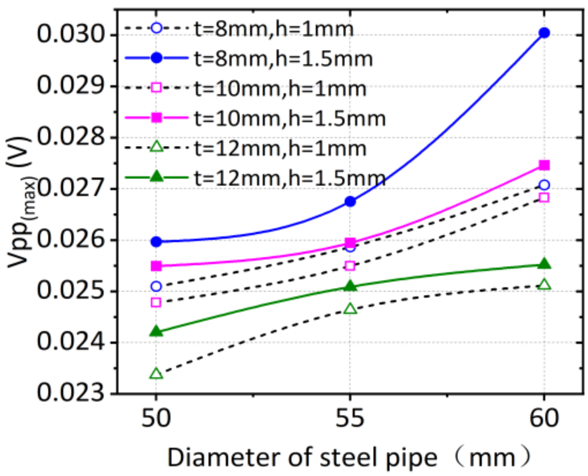

Figure 9. The influence of the external diameter on the signal.

As shown in Figure 9, the ΔVpp of the axial crack in the internal wall increases with the increase in the internal diameter of the steel pipe, and the ΔVpp values of the steel pipe with a wall thickness of 12 mm are the smallest. In addition, the signals of different depth defects with a change in the internal diameter of the pipe show the same trend, but the signal amplitude is more affected by the depth of the defect when the wall thickness is smaller, or the diameter of the pipe is larger.

The curve of signal amplitude versus wall thickness was redrawn as shown in Figure 10. The signal decreases with the increase in wall thickness under the condition of the same external diameter. In the process of increasing the wall thickness from 10 mm to 12 mm, the decrease degrees of the signal of the φ50 mm and φ55 mm steel pipes are smaller than that of the φ60 mm steel pipes. This indicates that the amplitude of the MPPT signal of the axial internal wall crack is more affected by wall thickness for the steel pipes with a larger diameter.

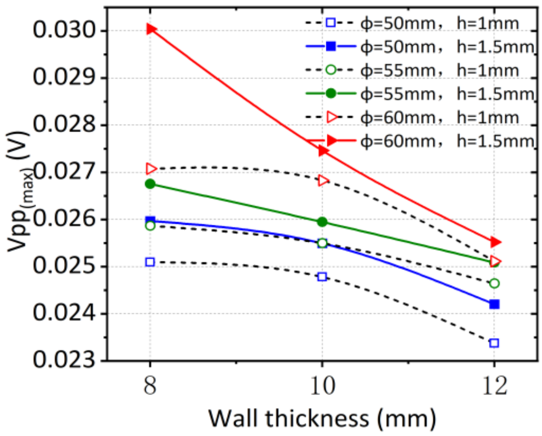

Figure 10. Detection signals at different wall thicknesses and external diameters.

4. Experiment and Results

4.1. Experimental Systems and Specimens

An MPPT system is designed to accommodate a wide range of steel pipe diameter specifications, as shown in Figure 11. The experimental setup consists of the following parts: a circumferential magnetizer, a DC power supply, sample pipes, a probe, and a signal acquisition and signal processing system. The magnetizer provides a magnetic field perpendicular to the direction of the defect. The probe sweeps through the sample pipe to output a signal, which is processed by a low-pass filter and signal amplifier to reduce background noise and amplify the output signal, and finally received by the signal acquisition module. In all experiments, the raw output voltages are processed using a tlc2262-based amplifier with a designed amplifier gain of 1000.

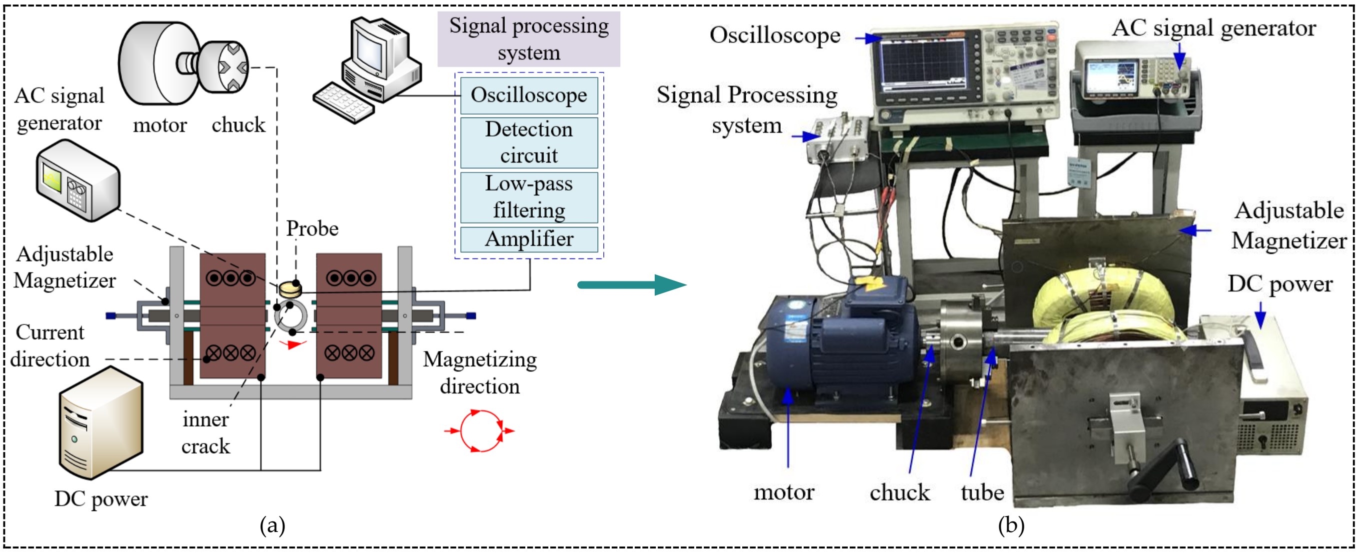

Figure 11. The MPPT system for the small-diameter thick-walled steel pipes. (**a**) is a diagram of the experimental platform model. (**b**) shows the experimental platform.

The test platform mainly contains three specifications of steel pipe specimens with diameters of φ50 mm, φ54 mm, and φ60 mm. The magnetic pole shoe in the testing device consists of a left pole shoe, a right pole shoe, and adjustable screws. In the experiment, in order to avoid the influence of the change in the distance between the pole shoe and the external wall of different pipes, the distance between the left and right pole shoes can be adjusted during the experiment to ensure that the minimum distance between the left and right pole shoes and the external wall of different specifications of the sample pipes is

5 mm, the width of the pole shoe is 25 mm, and the axial length along the sample pipe is 225 mm.

Six experimental sample pipes were used in the experiments, as shown in Figure 12. The axially scored grooves were scored using EDM. The crack length and width dimensions are 20 mm × 1 mm, and the depths are 0.5 mm, 1 mm, and 1.5 mm respectively.

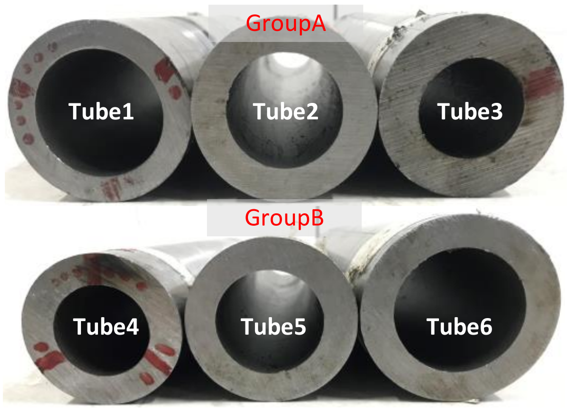

Figure 12. The specimens.

4.2. Feasibility of MPPT for Small-Diameter Thick-Walled Pipes

In order to verify the feasibility of the MPPT method for determining the axial cracks in the internal walls of steel pipes, a set of experiments was conducted on the axial cracks of small-diameter steel pipes. A tile-type differential probe was used for the test, as shown in Figure 13a, and the probe lift-off was 0.03 mm. In the experiment, the magnetization current was 17 A, the voltage of the excitation coil was 3 V, and the frequency was 40 kHz.

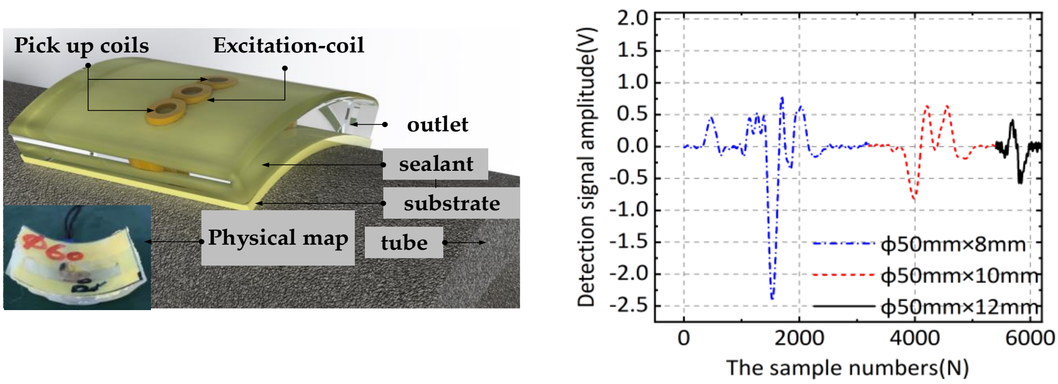

(a) (b)

Figure 13. (**a**) Probe structure. (**b**) Experimental signal.

Figure 13b shows the experimentally derived signals of the axial cracks in the steel pipes of different wall thicknesses. The results show that obvious detection signals can be obtained for defects at a depth of 1.5 mm in the internal walls of the three types of pipes, but the signal amplitude of the steel pipe with the smallest wall thickness is the largest.

4.3. Effect of External Diameter of Pipes on MPPT Signal

Experiments involving Group A were conducted for steel pipes with different external diameters. The external diameters of the pipes were 50 mm, 54 mm, and 60 mm, and all the wall thicknesses were 10 mm. The magnetizing current was 15 A in the experiments. The fitted curves of the peak-to-peak values of the internal axial crack signals for different pipes are shown in Figure 14.

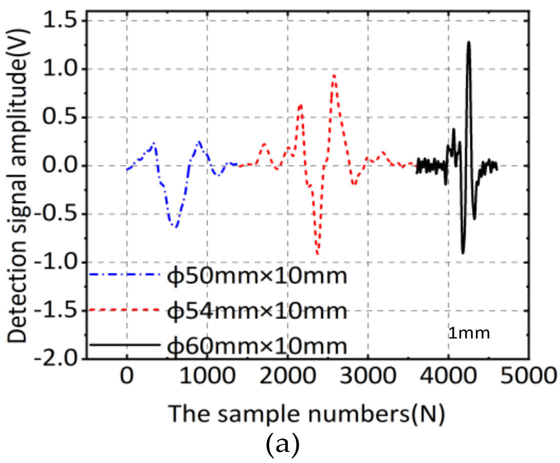

Figure 14. Experimental signals of group A. (**a**) Crack depth of 1 mm; (**b**) crack depth of 1.5 mm.

For internal axial cracks of the same size, as the external diameter of the pipe increases, the peak value of the experimental signal first increases and then tends to level off, as shown in Figure 15b. For cracks with different depths, the signal of the internal axial crack decreases significantly as the defect depth decreases. The trends of the experimental signals with the external diameter of the pipe for 1.5 mm depth and 1 mm depth defects are consistent with the simulation results.

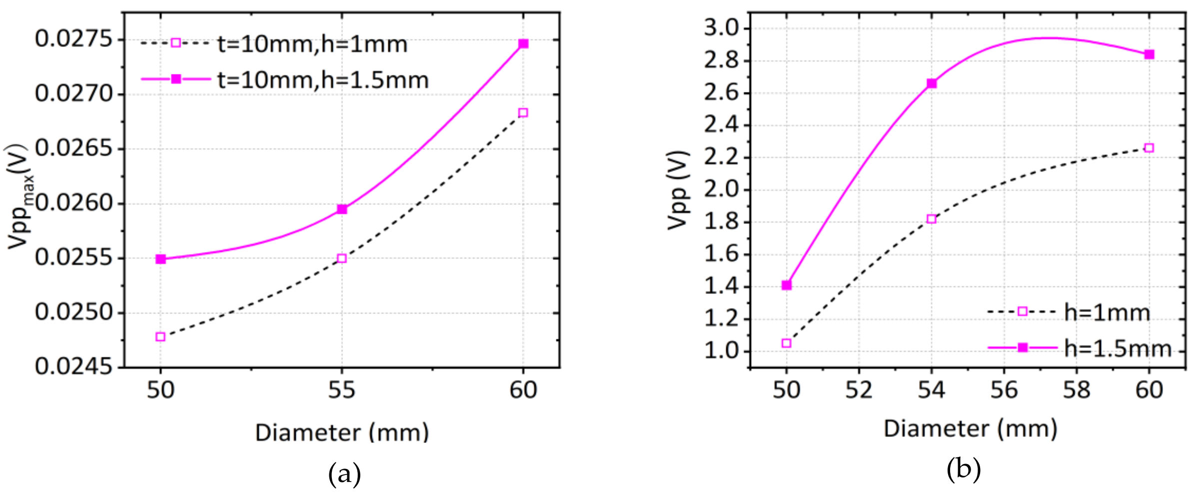

Figure 15. Signals for pipes of different external diameters. (**a**) Simulation results; (**b**) experimental results.

4.4. The Effect of Wall Thickness on the MPPT Signal

Experiments were conducted on Group B, consisting of steel pipes with the same external diameters and different wall thicknesses, to verify the effect of the internal diameter of a pipe on the MPPT signal. The signals of axial cracks in the internal walls of the pipes of different sizes are shown in Figure 15. Their peak-to-peak values were extracted, and the obtained fitted curves are shown in Figure 16.

As shown in the experimental results in Figure 17b, the signal amplitude of the defects at the same depth decreases with the increase in the pipe thickness. It can be inferred from the trend that when the wall thickness is less than 8 mm, the signal increases significantly with the increase in the defect depth. When the wall thickness is larger than 12 mm, the increase in defect depth may have little effect on the signal amplitude within a certain depth range.

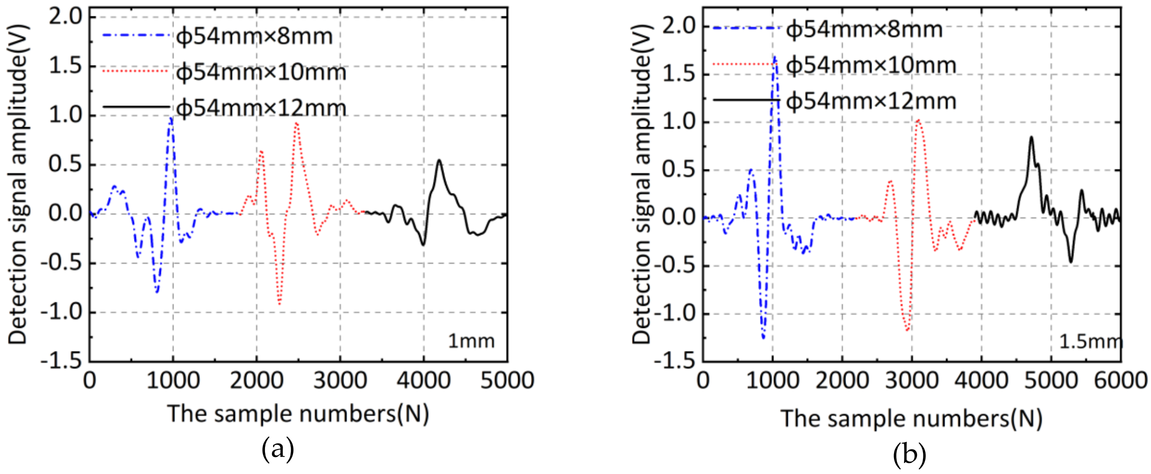

Figure 16. Experimental signals of group B. (**a**) Crack depth of 1 mm; (**b**) crack depth of 1.5 mm.

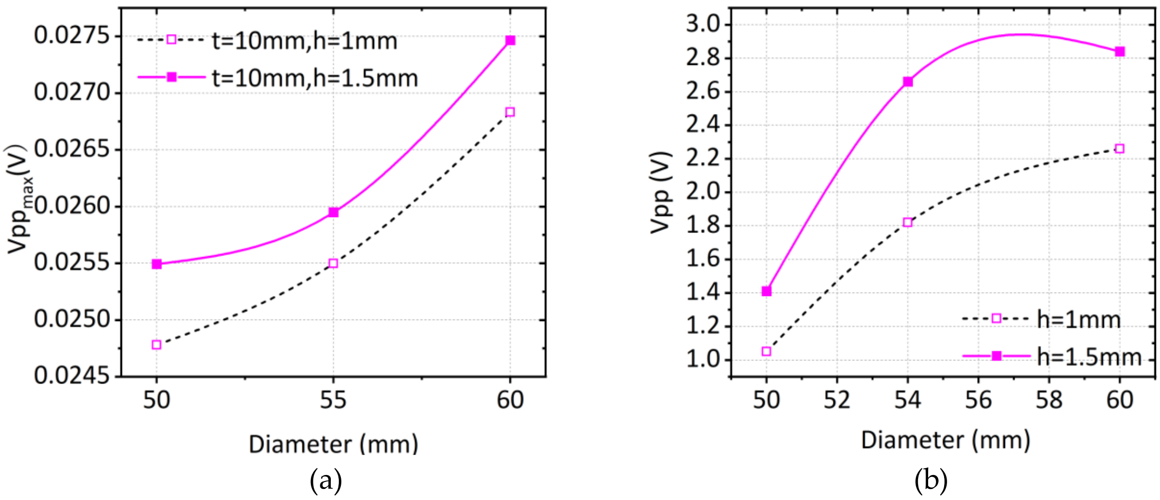

Figure 17. Signals for pipes of different internal diameters. (**a**) Simulation results; (**b**) experimental results.

5. Discussion

By using steel pipes of different diameters and thicknesses, more significant experimental signals were obtained and analyzed. The magnetic permeability perturbation of axial cracks in the internal wall of a steel pipe is determined by the internal diameter of the pipe, the wall thickness of the pipe, the magnetization state of the pipe, and the size of the defect. The increase in wall thickness and the decrease in pipe diameter will also affect the detection performance of this method. Even when in the same magnetization state and for defects with the same depth, different diameters will bring about differences in signal amplitude. For internal axial cracks with greater burial depths, the measurement of the weak MPP signal requires a probe with higher sensitivity. For the differential probe used in this method, both the external surface defects and internal surface defects can be detected, making it difficult to distinguish between the external and internal surface defects according to the signals. In the inspection process, as the thickness of the steel pipe increases, the difficulty of magnetization increases, and the volume of the magnetizer increases. Future work will focus on the optimization of the probe, the lightening of the magnetizer, and the differentiation of the MPPT signals between internal and external cracks.

6. Conclusions

In this paper, an MPPT method for detecting internal axial cracks in small-diameter thick-walled steel pipes was proposed. The surface MMP caused by axial cracks in the internal wall leads to an effective eddy current perturbation in the surface layer, which is sensed by the probe. Regarding the conventional MFL method, with the increase in wall thickness, the detection of internal wall defects becomes more difficult. However, the MPPT method offers better detection performance for small-diameter thick-walled pipes with a thickness-to-diameter ratio greater than 0.2. Both the simulation and experimental results have verified the method's feasibility. This method does not benefit from the lift-off effect, nor is it limited by the skin effect, giving it great practical value as a supplement to the evaluation of thick-walled steel pipes.

Author Contributions: Conceptualization, X.S.; methodology, Z.D.; software, T.L.; validation, T.L.; writing—original draft preparation, Z.Y. and X.Z.; writing—review and editing, Z.D.; funding acquisition, Z.D. All authors have read and agreed to the published version of the manuscript.

Funding: This research was funded by the National Natural Science Foundation of China, grant number 52105550; the National key research and development program, grant number 2022YFF0605600; and the Knowledge Innovation Project of Wuhan, grant number 2022010801020266.

Data Availability Statement: Not applicable.

Conflicts of Interest: The authors declare no conflict of interest.

References

1. Xu, J.; Lian, Z.; Hu, J.; Luo, M. Prediction of the Maximum Erosion Rate of Gas–Solid Two-Phase Flow Pipelines. *Energies* **2018**, *11*, 2773. [CrossRef]
2. Chen, C.; Li, C.; Reniers, G.; Yang, F. Safety and security of oil and gas pipeline transportation: A systematic analysis of research trends and future needs using WoS. *J. Clean. Prod.* **2020**, *279*, 123583. [CrossRef]
3. Zhang, T.; Li, Y.; Li, C.; Sun, S. Effect of salinity on oil production: Review on low salinity waterflooding mechanisms and exploratory study on pipeline scaling. *Oil Gas Sci. Technol.–Rev. D'ifp Energ. Nouv.* **2021**, *75*, 50. [CrossRef]
4. Zou, Y.; Du, D.; Chang, B.; Ji, L.; Pan, J. Automatic weld defect detection method based on Kalman filtering for real-time radiographic inspection of spiral pipe. *NDT E Int.* **2015**, *72*, 1–9. [CrossRef]
5. Yoon, B.; Kim, Y.; Yang, S. An experimental result on flaw sizing of steam generator tube at nuclear power plants using ultrasonic testing. *J. Nucl. Sci. Technol.* **2012**, *49*, 760–767. [CrossRef]
6. Marquez, F.P.G.; Muñoz, C.Q.G. A New Approach for Fault Detection, Location and Diagnosis by Ultrasonic Testing. *Energies* **2020**, *13*, 1192. [CrossRef]
7. Yang, Q.; Xie, S.; He, K.; Chen, Y.-E.; Chen, Z.; Uchimoto, T.; Takagi, T. A novel circumferential eccentric eddy current probe and its application for defect detection of small-diameter tubes. *Sens. Actuators A Phys.* **2021**, *331*, 113023. [CrossRef]
8. Kim, Y.-J.; Lee, S.-S. Eddy current probes of inclined coils for increased detectability of circumferential cracks in tubing. *NDT E Int.* **2012**, *49*, 77–82. [CrossRef]
9. Lysenko, I.; Kuts, Y.; Uchanin, V.; Protasov, A.; Petryk, V.; Alexiev, A. Using the Pulsed Eddy Current Techniques for Monitoring the Aircraft Structure Condition. *Trans. Aerosp. Res.* **2023**, *2023*, 22–31. [CrossRef]
10. Yang, B.; Li, X. Pulsed remote field technique used for nondestructive inspection of ferromagnetic tube. *NDT E Int.* **2013**, *53*, 47–52. [CrossRef]
11. Piao, G.; Guo, J.; Hu, T.; Deng, Y.; Leung, H. A novel pulsed eddy current method for high-speed pipeline inline inspection. *Sens. Actuators A Phys.* **2019**, *295*, 244–258. [CrossRef]
12. Sophian, A.; Tian, G.; Fan, M. Pulsed Eddy Current Non-destructive Testing and Evaluation: A Review. *Chin. J. Mech. Eng.* **2017**, *30*, 500–514. [CrossRef]
13. Kako, M.; Tomizawa, T.; Ge, J.; Ruan, X.; Nozawa, T.; Yusa, N. The applicability of remote field eddy current testing to outer flaws on cooling tubes in the blanket of a fusion DEMO reactor. *Fusion Eng. Des.* **2023**, *194*, 113709. [CrossRef]
14. Kobayashi, N.; Ueno, S.; Nagai, S.; Ochiai, M.; Jimbo, N. Remote field eddy current testing for steam generator inspection of fast reactor. *Nucl. Eng. Des.* **2011**, *241*, 4643–4648. [CrossRef]
15. Thirunavukkarasu, S.; Arjun, V.; Rao, B.P.C.; Mukhopadhyay, C.K. Development of a High-Sensitive Dual Frequency Remote Field Eddy Current Instrument for Inspection of Ferromagnetic Steam Generator Tubes. *IETE Tech. Rev.* **2019**, *36*, 203–208. [CrossRef]
16. Xiao, Q.; Feng, J.; Xu, Z.; Zhang, H. Receiver Signal Analysis on Geometry and Excitation Parameters of Remote Field Eddy Current Probe. *IEEE Trans. Ind. Electron.* **2022**, *69*, 3088–3098. [CrossRef]
17. Liu, B.; He, L.-Y.; Zhang, H.; Cao, Y.; Fernandes, H. The axial crack testing model for long distance oil-gas pipeline based on magnetic flux leakage internal inspection method. *Measurement* **2017**, *103*, 275–282. [CrossRef]
18. Parra-Raad, J.A.; Roa-Prada, S. Multi-Objective Optimization of a Magnetic Circuit for Magnetic Flux Leakage-Type Non-destructive Testing. *J. Nondestruct. Eval.* **2016**, *35*, 14. [CrossRef]

19. Pham, H.Q.; Le, V.S.; Vu, M.H.; Doan, D.T.; Tran, Q.H. Design of a lightweight magnetizer to enable a portable circumferential magnetic flux leakage detection system. *Rev. Sci. Instrum.* **2019**, *90*, 074705. [CrossRef]
20. Singh, W.S.; Mukhopadhyay, C.K.; Rao, B.P.C. Development of a high sensitive magnetic flux leakage instrument for imaging of localised flaws in small diameter ferromagnetic steel tubes. *IET Sci. Meas. Technol.* **2018**, *12*, 932–936. [CrossRef]
21. Wu, D.; Liu, Z.; Wang, X.; Su, L. Composite magnetic flux leakage detection method for pipelines using alternating magnetic field excitation. *NDT E Int.* **2017**, *91*, 148–155. [CrossRef]
22. Durai, M.; Lan, C.-W.; Chang, H. In-line detection of defects in steel pipes using flexible GMR sensor array. *J. King Saud Univ.-Sci.* **2022**, *34*, 101761. [CrossRef]
23. Cheng, S.; Wu, X.; Kang, Y. Local area magnetization and inspection method for aerial pipelines. *NDT E Int.* **2005**, *38*, 448–452. [CrossRef]
24. Pei, C.; Xiao, P.; Zhao, S.; Chen, Z.; Takagi, T. A flexible film type EMAT for inspection of small diameter pipe. *J. Mech. Sci. Technol.* **2017**, *31*, 3641–3645. [CrossRef]
25. Tu, J.; Zhong, Z.; Song, X.; Zhang, X.; Deng, Z.; Liu, M. An external through type RA-EMAT for steel pipe inspection. *Sens. Actuators A Phys.* **2021**, *331*, 113053. [CrossRef]
26. Capponi, C.; Brunone, B.; Maietta, F.; Meniconi, S. Hydraulic Diagnostic Kit for the Automatic Expeditious Survey of in-line Valve Sealing in Long, Large Diameter Transmission Mains. *Water Resour. Manag.* **2023**, *37*, 1931–1945. [CrossRef]
27. Brunone, B.; Capponi, C.; Meniconi, S. Design criteria and performance analysis of a smart portable device for leak detection in water transmission mains. *Measurement* **2021**, *183*, 109844. [CrossRef]
28. Deng, Z.; Yu, Z.; Yuan, Z.; Song, X.; Kang, Y. Mechanism of Magnetic Permeability Perturbation in Magnetizing-Based Eddy Current Nondestructive Testing. *Sensors* **2022**, *22*, 2503. [CrossRef]
29. Gotoh, Y.; Sakurai, K.; Takahashi, N. Electromagnetic Inspection Method of Outer Side Defect on Small and Thick Steel Tube Using Both AC and DC Magnetic Fields. *IEEE Trans. Magn.* **2009**, *45*, 4467–4470. [CrossRef]
30. Sophian, A.; Tian, G.Y.; Taylor, D.; Rudlin, J. Flaw detection and quantification for ferromagnetic steels using pulsed eddy current techniques and magnetization. In *WIT Transactions on Engineering Sciences*; WIT Press: Ashurst, UK, 2003.
31. Li, E.; Wu, J.; Zhu, J.; Kang, Y. Quantitative Evaluation of Buried Defects in Ferromagnetic Steels Using DC Magnetization-Based Eddy Current Array Testing. *IEEE Trans. Magn.* **2020**, *56*, 6200811. [CrossRef]
32. Wu, J.; Zhu, J.; Xu, Z.; Xia, H. A DC-Biased Scanning Induction Thermographic System for Characterizing Surface Cracks in Ferromagnetic Components. *IEEE/ASME Trans. Mechatron.* **2021**, *26*, 2782–2790. [CrossRef]